Original Research

Comparative study of wild-type and rd10 mice reveals transient intrinsic optical signal response before phosphodiesterase activation in retinal photoreceptors

Yiming Lu[1], Tae-Hoon Kim[1] and Xincheng Yao[1,2]

[1]Department of Bioengineering, University of Illinois at Chicago, Chicago, IL 60607, USA; [2]Department of Ophthalmology and Visual Sciences, University of Illinois at Chicago, Chicago, IL 60612, USA
Corresponding author: Xincheng Yao. Email: xcy@uic.edu

Impact statement

Comparative study of wild-type and rd10 mice was implemented to reveal that transient intrinsic optical signal (IOS) was initiated before the phosphodiesterase activation in stimulus-activated photoreceptors and the IOS magnitude was sensitive to photoreceptor degeneration. The photoreceptor-IOS promises a noninvasive biomarker for objective assessment of age-related macular degeneration, retinitis pigmentosa, and other eye diseases that can produce photoreceptor dysfunctions.

Abstract

Transient intrinsic optical signal (IOS) has been observed in stimulus-evoked retinal photoreceptors. This study is to compare IOS changes in wild-type and retinal degeneration 10 (rd10) mouse retinas, to evaluate the effect of cyclic guanosine monophosphate phosphodiesterase on photoreceptor-IOS. Time-lapse near-infrared light microscopy was employed to monitor the spatiotemporal dynamics of the IOS responses in freshly isolated retinas activated by visible light stimulation. Comparative IOS recordings were conducted at postnatal days 14 (P14) and P16. At P14, intrinsic optical signal magnitudes and spatiotemporal dynamics in wild-type and rd10 retinas were similar, indicating that the phosphodiesterase deficiency in rd10 did not affect the formation of photoreceptor-IOS. At P16, IOS magnitude in rd10 significantly decreased compared to that in wild-type, suggesting the IOS sensitivity to the photoreceptor degeneration in rd10. Our experimental results and theoretical analysis indicate that early disc-based stages of the phototransduction cascade before the activation of phosphodiesterase may contribute to the formation of the photoreceptor-IOS responses; and the IOS can be a sensitive biomarker for objective assessment of retinal function.

Keywords: Intrinsic optical signal, functional imaging, retinal degeneration, photoreceptors, rd10, phosphodiesterase deficiency

Experimental Biology and Medicine **2020; 245: 360–367. DOI: 10.1177/1535370219896284**

Introduction

Functional assessment of retinal physiology is important for early detection and treatment assessment of eye diseases, such as age-related macular degeneration (AMD), diabetic retinopathy (DR), and retinitis pigmentosa (RP).[1–3] Electroretinogram (ERG) can be used for objective evaluation of the retinal function. However, it provides limited spatial resolution and signal specificity.[4] Intrinsic optical signal (IOS) imaging of retina measures the stimulus-evoked intrinsic optical property changes, such as light scattering, polarization, and absorption fluctuation, in the retina activated by visible light stimulation.[5] In conjunction with advanced imaging technologies, such as optical coherence tomography (OCT), scanning laser ophthalmoscopy (SLO) and adaptive optics, functional IOS imaging promises a noninvasive, objective, and high-resolution method to evaluate retinal physiological function.[6–8]

Retinal IOS responses have been demonstrated in different animal models and human eyes with various optical imaging modalities.[9–12] Rapid IOS has been consistently observed in retinal photoreceptors, and slow IOS changes have been reported correlated with inner retinal neural response and hemodynamics.[7] The photoreceptor-IOS occurs almost right away, < 4 ms after the initiation of retinal stimulation.[13,14] Transient photoreceptor outer segment (OS) changes have been demonstrated to have a close correlation with the rapid photoreceptor-IOS.[10,15] Comparative ERG study of freshly isolated retina further

revealed that such conformational changes happen before the hyperpolarization of the photoreceptors.[16] These experimental observations suggest that the rapid photoreceptor-IOS has a physiological origin in the upstream, disc-based phototransduction cascade steps, including the sequential activation of rhodopsin, transducin, and cyclic guanosine monophosphate (cGMP) phosphodiesterase (PDE).[17–19]

In this study, a retinal degeneration mouse model *Pde6b*^{rd10} (rd10) was used to test if the PDE is involved in the production of transient photoreceptor-IOS. The rd10 mouse model has a spontaneous mutation in the gene of the β-subunit of PDE (β-PDE) in the rod photoreceptors.[20] The deficiency of PDE causes the accumulation of cGMP and results in the degeneration of rod photoreceptors due to the excessive influx of cations. However, as the rods still express <40% of endogenous PDE in the rd10 mouse, it has a relatively delayed onset of photoreceptor degeneration.[20] Before postnatal days 15 (P15), the relative expression level of rhodopsin and transducin in rd10 mouse is similar with that in the wild-type (WT) mouse. Additionally, the difference between relative cell death ratios in WT and rd10 mouse is also insignificant in the first two postnatal weeks.[20,21] In comparison, the relative expression level of PDE in rd10 mouse is about 21%–28% of that in the WT mouse during P12–P14.[20] Therefore, a comparative study between WT and rd10 mice before P15 can specifically reveal the effect of PDE deficiency on the photoreceptor-IOS. WT and rd10 mice at P14 were selected for comparative IOS imaging study to test the effect of PDE on the photoreceptor-IOS. Furthermore, the retinal degeneration process in rd10 mouse starts from P16 to P18.[20–23] Thereafter, the relative expression level of rhodopsin and transducin significantly decreases in the rd10 mouse compared to that in the WT mouse. Histological changes of the retina have been consistently observed in rd10 mouse since P16.[24,25] To demonstrate the impact of early retinal degeneration process on the photoreceptor-IOS, comparative IOS imaging study of WT and rd10 retinas at P16 was conducted.

Materials and methods

Experimental setup

Figure 1 illustrates the schematic diagram of the experimental setup. The imaging system is based on a modified NIR light microscope (BX531WI, Olympus) with a 60× objective lens (LUMPLanFL60X, NA 0.9, Olympus). A fiber-coupled light emitting diode (LED) at visible wavelength (center wavelength: 550 nm, bandwidth: ~200 nm) was used to provide retinal stimulation. The stimulus light was collimated and then coupled into the microscope. A slit with its conjugate plane at the sample plane was

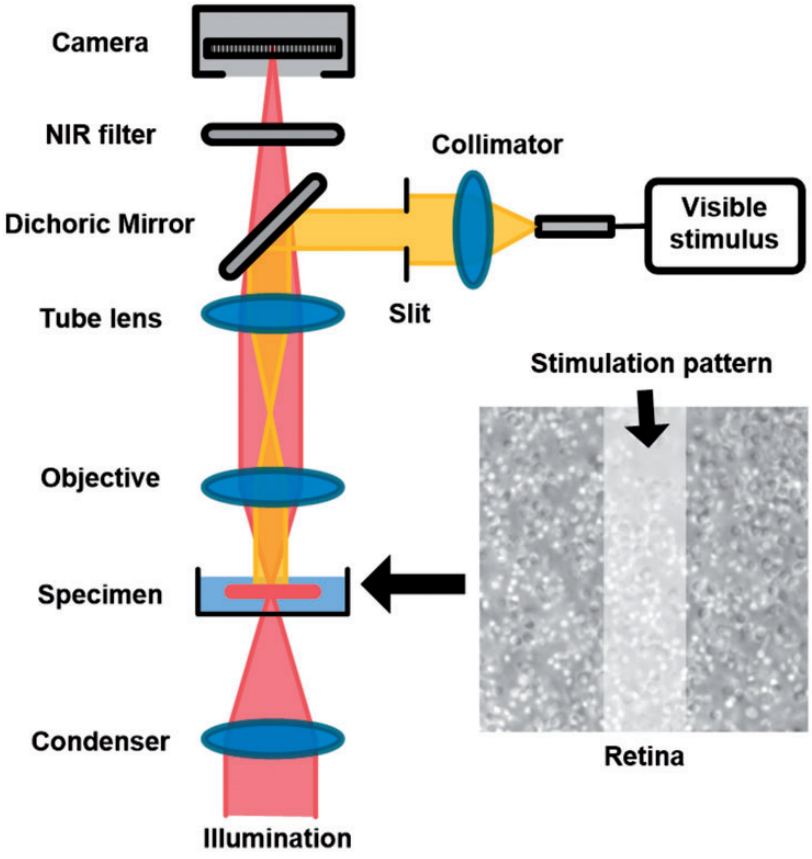

Figure 1. Schematic diagram of the experiment setup. A custom modified microscope, with a 60× objective and a CMOS camera (16 bits depth and 100 frames/s), was used for retinal imaging. During the experiment, the photoreceptor outer segment (OS) tips were facing upward and the retina was perfused with oxygenated physiological solution (pH 7.4 and 35–37°C). A rectangular stimulus pattern, generated by a slit and a LED at visible wavelength, was projected to the retina for localized stimulus. The stimulus duration was 500 ms for all the experiments. (A color version of this figure is available in the online journal.)

employed to generate a rectangular stimulus pattern ($\sim$12 μm × 56 μm) at the center of the field of view. The stimulus intensity was set to $\sim 3.6 \times 10^9$ photon/μm^2/s with a duration of 500 ms during the experiment. A perfusion system was employed to perfuse the retina with oxygenated bicarbonate-buffered Ames medium (pH 7.4 and 35–37°C) during the experiment. The perfusion was suspended during the image recording to minimize the effect of fluid fluctuation on the image quality. The retinal images were recorded by a CMOS camera (pixel size: 6.5 μm ×6.5 μm, Neo 5.5, Andor Technology) with an imaging speed of 100 frames/s and a frame resolution of 512 × 512 pixels. The stimulus light source and the image recording system were electronically synchronized and controlled by a custom-designed LabView (National Instrument) platform.

Sample preparation

WT mice (57BL/6J, The Jackson Laboratory) and rd10 mice (B6.CXB1-Pde6b^{rd10}/J, The Jackson Laboratory) at P14 and P16 were used in this study. Both WT and rd10 mice were maintained in standard housing conditions under a 14/10-h light-dark cycle. For each postnatal day, 12 WT mice and 12 rd10 mice with no significant difference in body size and weight were selected for experiments. All the mice were dark-adapted for more than 6 h before the experiment. The isolation of mouse retina has been reported in our previous study.[26] Briefly, enucleated eyeball from anesthetized mouse was hemisected along the equator with fine scissors. The retina was then carefully isolated from the retinal pigment epithelium (RPE) and separated from the back of the eye. The isolated retina was transferred to a chamber for IOS imaging with the OS tip of the photoreceptor facing upward. As the photoreceptors degenerate first in rd10 mouse model, such setup allows an unambiguous identification of the structural change of photoreceptors and a reliable identification of the IOS responses from photoreceptors. All the procedures were performed in oxygenated bicarbonate-buffered Ames medium (pH 7.4 and 35–37°C). To ensure the consistency of the observations, retinal images were all acquired from the retinal locations close to the optical nerve head (ONH)[22] and the imaging plane was focused at the photoreceptor OS layer. All the procedures were conducted in a dark room with minimum level of red-light illumination.

For histological study of mouse retinas, the mice at P14 and P16 were euthanized by carbon dioxide (CO_2) inhalation, followed by enucleation for both eyes. The eyeball was immediately embedded in tissue freezing medium and placed on dry ice prior to cryostat sectioning. The cryostat sectioning (10 μm in thickness) was performed to harvest retinal tissues near the ONH. The sections were subsequently fixed with 4% paraformaldehyde (PFA) and 1% glutaraldehyde (GA) for 15 min. After washing the fixative solution with 1×PBS, hematoxylin (ab245880, Abcam) was applied and incubated for 5 min. The hematoxylin was then rinsed in two changes of distilled water prior to OS length measurement under a microscope. To ensure the reliability of the data, OS lengths were measured at $\sim$350 μm from the ONH in all samples where the thickness of retina is relatively consistent.

All experiments were performed following the protocols approved by the Animal Care Committee (ACC) at the University of Illinois at Chicago and conformed to the statement on the use of animals in ophthalmic and vision research, established by the Association for Research in Vision and Ophthalmology (ARVO).

Data processing

Figure 2 shows representative retinal images and corresponding IOS maps. Each recording trial contains three phases, a 1.0-s pre-stimulus phase, a 0.5-s stimulus phase, and a 3.5-s post-stimulus phase. The IOS can be processed based on the retinal images

$$IOS_t(x,y) = \frac{|\Delta I_t(x,y)|}{\bar{I}_{pre}(x,y)} = \frac{|I_t(x,y) - \bar{I}_{pre}(x,y)|}{\bar{I}_{pre}(x,y)}$$

where $IOS_t(x,y)$ represents the IOS map with a frame index of t, $-I_{pre}(x,y)$ represents the mean intensity map of all images recorded during the pre-stimulus phase, and $I_t(x,y)$ is the retinal image with a frame index of t. A 3-δ threshold and a temporal window filter were applied to suppress potential spatial and temporal noise contributions to the IOS map. For the 3-δ threshold, a pixel with coordinate $(x_k,\ y_k)$ in a retinal image $I_t(x,y)$ will be regarded as reflecting IOS when $I_t(x_k,\ y_k) > -I_{pre}(x_k,\ y_k) + 3 \cdot \delta_{pre}(x_k,\ y_k)$ or $I_t(x_k,\ y_k) < -I_{pre}(x_k,\ y_k) - 3 \cdot \delta_{pre}(x_k,\ y_k)$, where $\delta_{pre}(x_k,\ y_k)$ is the standard deviation of all pre-stimulus images. For the temporal window filter with an n-frame window size, $I_t(x_k,\ y_k) \ldots I_{t+n}(x_k,\ y_k)$ should consistently meet the 3-δ threshold to include $I_t(x_k,\ y_k)$ for IOS calculation. In this study, $n = 3$ was used considering the signal-to-noise ratio of IOS responses.

Results

Figure 2(a) shows a representative sequence of retinal images acquired from a P16 WT mouse. Individual photoreceptor OS tips can be clearly identified. Figure 2(b) shows the corresponding photoreceptor-IOS image sequence. Each illustrated frame is an average of 50 photoreceptor-IOS maps acquired during the 0.5-s interval. Figure 2(c) shows the sequence of immediate photoreceptor-IOS responses after the onset of stimulus at a temporal resolution of 10 ms. As shown in Figure 2(c), rapid photoreceptor-IOS occurred almost immediately, within 10 ms after the onset of stimulus. Moreover, the photoreceptor-IOS intensities increased and its spatial distribution broadened over time. To quantify the temporal dynamics of photoreceptor-IOS responses, a magnitude-time curve of photoreceptor-IOS responses was obtained by averaging the photoreceptor-IOS intensities in each photoreceptor-IOS map and aligning them together following the time sequence (Figure 2(d)). The waveform of the curve shows that the flash stimulus evoked a robust photoreceptor-IOS with a peak at $\sim$0.4 s. Additionally, the photoreceptor-IOS

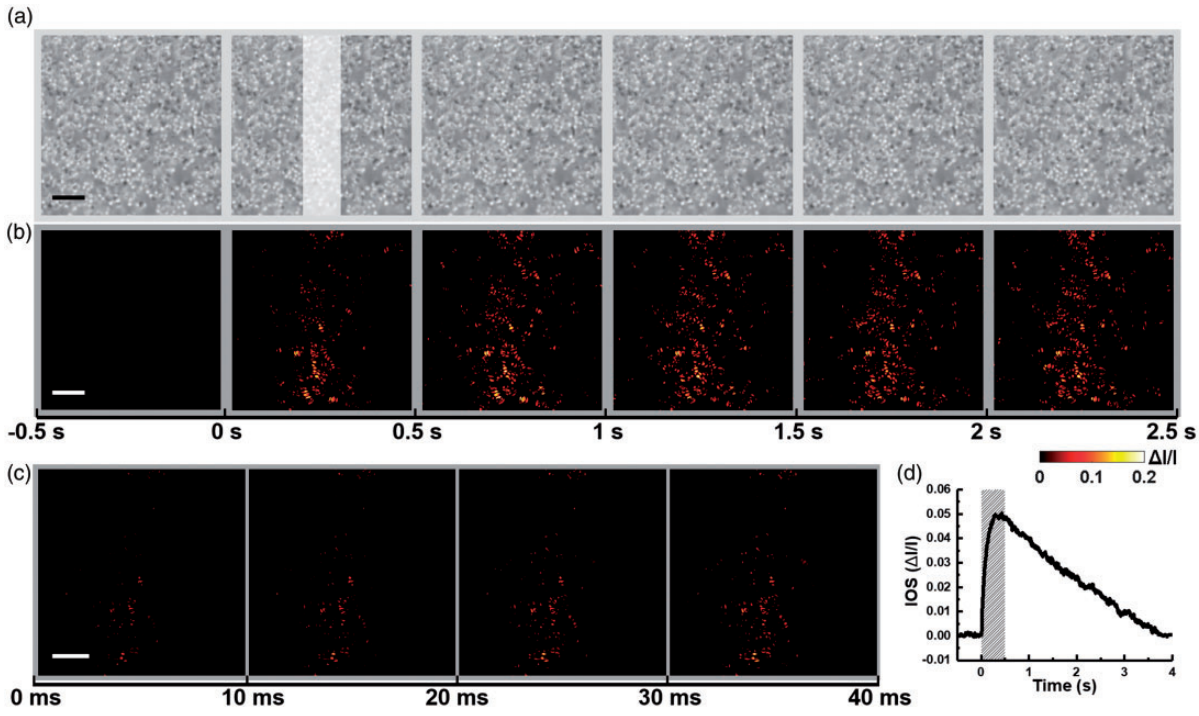

Figure 2. (a) Representative microscopic images of a P16 WT mouse retina acquired with a 0.5-s interval. The white rectangle in the second frame shows the visible stimulus pattern with a duration of 0.5 s. (b) Temporal sequence of photoreceptor-IOS maps corresponding to the data in (a). Each panel represents an average of all 50 photoreceptor-IOS maps acquired during the 0.5-s interval indicated by the time axis at the bottom. (c) Enlarged single-frame photoreceptor-IOS maps acquired after the onset of stimulus with an imaging speed of 100 frames/s. The time axis at the bottom indicates the acquisition time. (d) Time course of the mean magnitude of photoreceptor-IOS responses. The shaded area indicates the stimulus duration. Scale bars represent 10 μm. (A color version of this figure is available in the online journal.)

intensities gradually recovered to baseline in the post-stimulus phase.

To test the effect of PDE deficiency on the photoreceptor-IOS formation, we performed comparative studies of WT and rd10 mice at P14 (Figure 3(a) and (b)) and P16 (Figure 3 (c) and (d)). At P14, the overall structure of photoreceptors remained similar between WT and rd10 mice (Figure 3(a1) and (b1)). The spatial distribution of photoreceptor-IOS responses in both groups was mainly confined within the stimulus pattern, and the photoreceptor-IOS magnitudes were also relatively similar (Figure 3(a2) and (b2)). Figure 3(a3) and (b3) shows the time courses of the photoreceptor-IOS magnitude values. Photoreceptor-IOS waveforms in both WT and rd10 presented a flat stage prior to flash delivery, a rapid rise upon the initiation of the flash stimulus, a peak before the shutoff of the stimulus, and a recovery to baseline at ~2 s. The similarities between Figure 3(a2) and (b2) and (a3) and (b3) indicate that the PDE deficiency in rd10 mouse retina did not affect the formation of photoreceptor-IOS responses.

As shown in Figure 3(c1) and (d1), differences between the photoreceptor structures in WT and rd10 mouse retinas emerged at P16. Though some photoreceptor tips can still be identified in the rd10 mouse retina at P16, the spatial distribution and intensity of photoreceptor-IOS responses exhibited significant attenuation in the rd10 mouse retina (Figure 3(d2)), compared to that in WT mouse retina (Figure 3(c2)). The magnitude-time curve of photoreceptor-IOS responses in rd10 mouse retina (Figure 3(d3)) also shows a significantly lower peak value, compared to that in WT mouse retina (Figure 3(c3)).

To further confirm the observation, we repeated the experiment on 12 WT and 12 rd10 mice retinas at both P14 and P16, including the retinas shown in Figure 3. The results are shown in Figure 4. In each panel of Figure 4(a) and (c), the solid curve is the mean of all photoreceptor-IOS magnitude-time curves from 12 retinas and the accompanied colored area represents the standard deviations of data about the mean. For all the IOS data, the relationship of the standard deviation amplitudes to the mean waveform indicates a general similarity of the results obtained from different retinas. As the waveforms shown in Figure 4(a1) and (a2), the photoreceptor-IOS responses in WT and rd10 mouse retinas were similar at P14. However, the WT mouse retinas showed significantly stronger photoreceptor-IOS responses than rd10 mouse retinas at P16. To better demonstrate the similarity/difference of photoreceptor-IOS responses between WT and rd10 group at each postnatal day, peak amplitude (the maximum value of the IOS magnitude) and time-to-peak (time taken to reach the peak amplitude) of the photoreceptor-IOS waveforms were statistically analyzed. The results in Figure 4(b1) and (b2) show that there was no significant photoreceptor-IOS difference between WT and rd10 mice at P14. For P16, the photoreceptor-IOS peak amplitudes of WT mice retinas were significantly higher than that in the rd10 mice retinas (Figure 4(d1)), while the time-to-peaks still showed no significant difference (Figure 4(d2)).

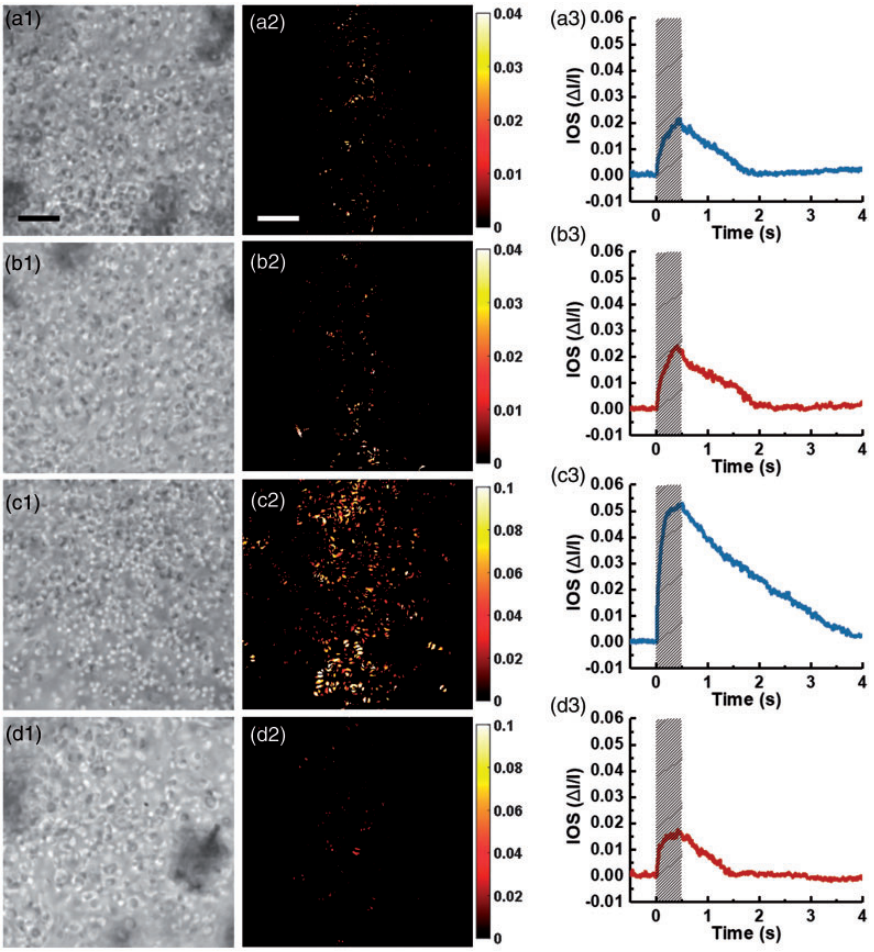

Figure 3. Comparison of photoreceptor-IOS responses between WT and rd10 groups at P14 and P16. (a) Representative retinal images (left) and photoreceptor-IOS map obtained at 0.5 s (middle), and time course of mean photoreceptor-IOS magnitude (right), acquired from a WT mouse retina at P14. (b) Representative results acquired from a rd10 mouse retina at P14. (c) Representative results acquired from a WT mouse retina at P16. (d) Representative results acquired from an rd10 mouse retina at P16. Scale bars represent 10 μm. Shaded areas indicate stimulus duration. (A color version of this figure is available in the online journal.)

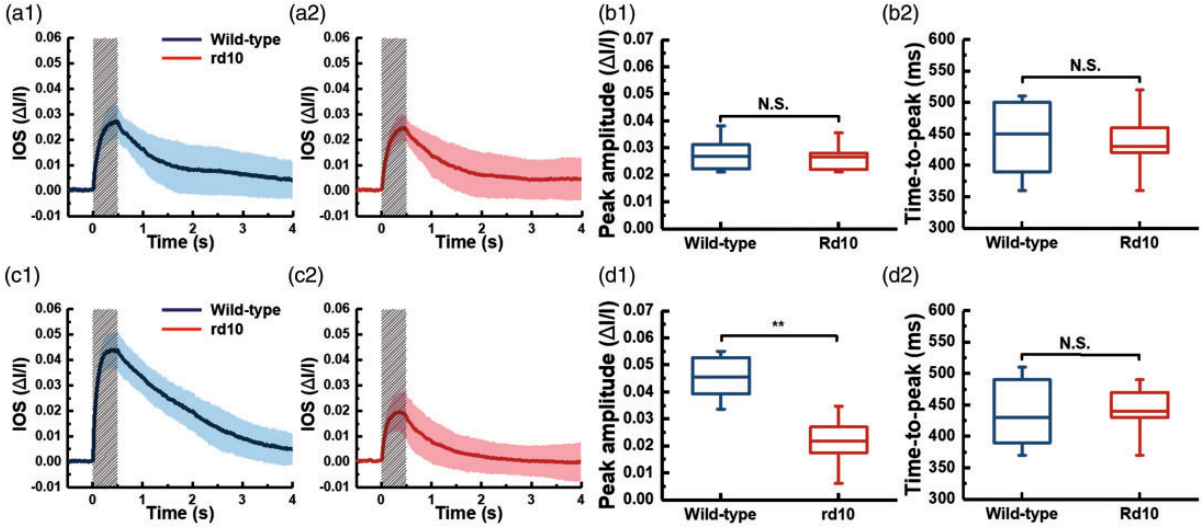

Figure 4. Averaged photoreceptor-IOS responses from WT and rd10 mice at P14 and P16 and the corresponding statistical characterization. Averaged magnitude-time curve of photoreceptor-IOS responses from 12 WT mouse retinas (a1) and 12 rd10 mouse retinas (a2) at P14. (b1) and (b2) are statistics of peak amplitudes and time-to-peaks corresponding to the data shown in (a1) and (a2), respectively ($n = 12$, N.S. = not significant). Averaged magnitude-time curve of photoreceptor-IOS responses from 12 WT mouse retinas (c1) and 12 rd10 mouse retinas (c2) at P16. (d1) and (d2) are statistics of peak amplitudes and time-to-peaks corresponding to the data shown in (c1) and (c2), respectively ($n = 12$, N.S. = not significant, $^{**}P < 0.05$). Significance was determined by a two-sample t-test with equal variance assumed. The normality of data was determined using the Kolmogorov–Smirnov test. Each solid curve in (a) and (c) represents the mean values, and the accompanied colored area represents the corresponding standard deviations, of the photoreceptor-IOS responses. The gray shaded areas represent stimulus duration. (A color version of this figure is available in the online journal.)

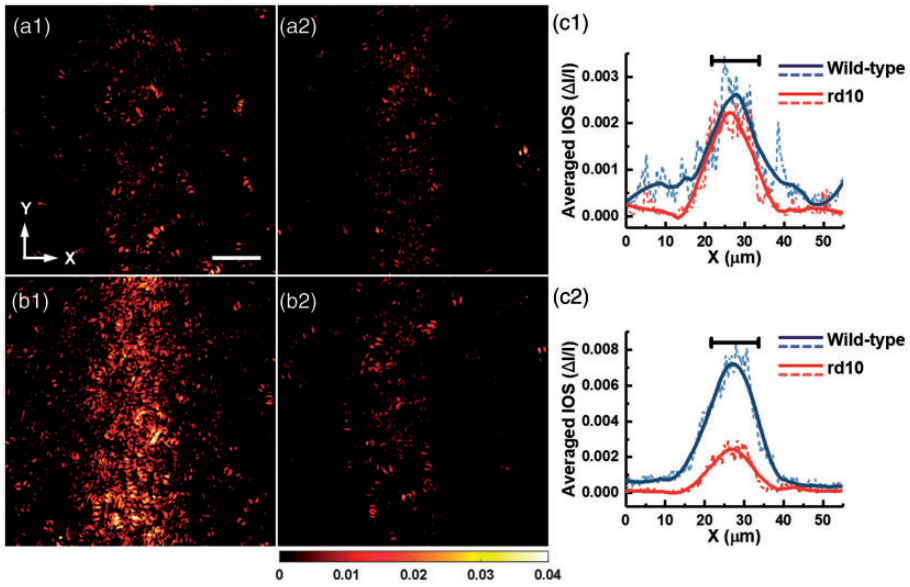

Figure 5. Averaged photoreceptor-IOS maps acquired at 0.5 s after the onset of stimulus from WT and rd10 mice. Each panel is an average of photoreceptor-IOS maps from 12 retinal samples. Averaged photoreceptor-IOS map of WT (a1) and rd10 (a2) mice at P14, and WT (b1) and rd10 mice (b2) at P16. (c) Intensity profiles of the photoreceptor-IOS maps averaged along Y-direction. The dashed curves represent the raw profiles of the mean intensity. The solid curves represent the corresponding profiles smoothed by 40 points. Mean intensity profiles of WT and rd10 mice at P14 (c1) and P16 (c2). The black bars at the top represent the width of the stimulus pattern (~12 μm). (A color version of this figure is available in the online journal.)

The results are consistent with the previous observations in Figure 3.

Figure 5 shows the averaged photoreceptor-IOS maps in WT and rd10 groups at time 0.5 s. Each panel in Figure 5 shows averaged data from 12 retina samples. At P14, the spatial distribution of photoreceptor-IOS responses in WT group (Figure 5(a1)) was similar to that in rd10 group (Figure 5(a2)). The majority of the active pixels are within the stimulus pattern. At P16, the distribution of photoreceptor-IOS responses in the WT group appeared wider in the X-direction and presented overall higher intensities compared to the rd10 group. To better quantify the difference in the spatial distribution of photoreceptor-IOS responses, each panel was averaged in the Y-direction and converted as an intensity profile in the X-direction (dashed curves in Figure 5(a3) and (b3)). To better show the spatial distribution of photoreceptor-IOS responses, the intensity profiles were smoothed by an empirical 40-point rolling window (solid curves in Figure 5(a3) and (b3)) with which the background perturbations can be sufficiently reduced but the overall shape of the profile can be reasonably maintained. At P14, the full-width-half-maximum (FWHM) values of the smoothed photoreceptor-IOS intensity profiles in WT and rd10 group are ~14.6 μm and ~14.2 μm, respectively. At P16, the FWHM values of the smoothed photoreceptor-IOS intensity profiles for WT and rd10 group are ~14.8 μm and ~12.35 μm, respectively. The results show that the spatial distributions of the photoreceptor-IOS responses in WT and rd10 group were similar at P14. But at P16, the spatial distribution of the photoreceptor-IOS responses in rd10 was compressed compared to that in WT group.

Histological examinations were further performed to demonstrate the structure of photoreceptor OSs in the intact retinas of WT and rd10 mice at P14 and P16 (Figure 6). Figure 6(a1) and (a2) shows the representative transmission light microscopic images of eyecup slices from WT and rd10 mice at P14, respectively. Figure 6(b1) and (b2) shows the representative images acquired from WT and rd10 mice at P16. The junctions of OS tips and RPE in Figure 6(a) and (b) were horizontally aligned (marked by the red-dashed line). The black-dashed lines correspond to the general position of OS/IS junctions. As shown in Figure 6(a1) and (a2), the OS layers of WT and rd10 mice at P14 present a general similarity in thickness. At P16, the thickness of OS layer in rd10 retina was reduced compared to that in WT retina (Figure 6(b1) and (b2)). To confirm these observations, OS lengths were measured from different retinal samples ($n = 6$ for each group). The results are shown in Figure 6(a3) and (b3). The statistical analysis reveals that the OS lengths are similar in WT and rd10 groups at P14. At P16, the rd10 group presented significantly reduced OS lengths compared with that in WT group.

Discussion

In this study, we compared the IOS responses in WT and rd10 retinas at P14 to investigate the effect of PDE deficiency on the photoreceptor-IOS formation. As the rod degeneration starts at around P16 in rd10 mouse, comparative photoreceptor-IOS imaging at P14 can isolate the impact of PDE deficiency from other degeneration factors (P15 was not considered to avoid the potential overlap with the degeneration process). A key observation was that the photoreceptor-IOS responses in rd10 mice were similar with that in WT mice at P14. As shown in Figure 4(a), the overall waveform of the mean photoreceptor-IOS curve and the amplitudes of the corresponding standard

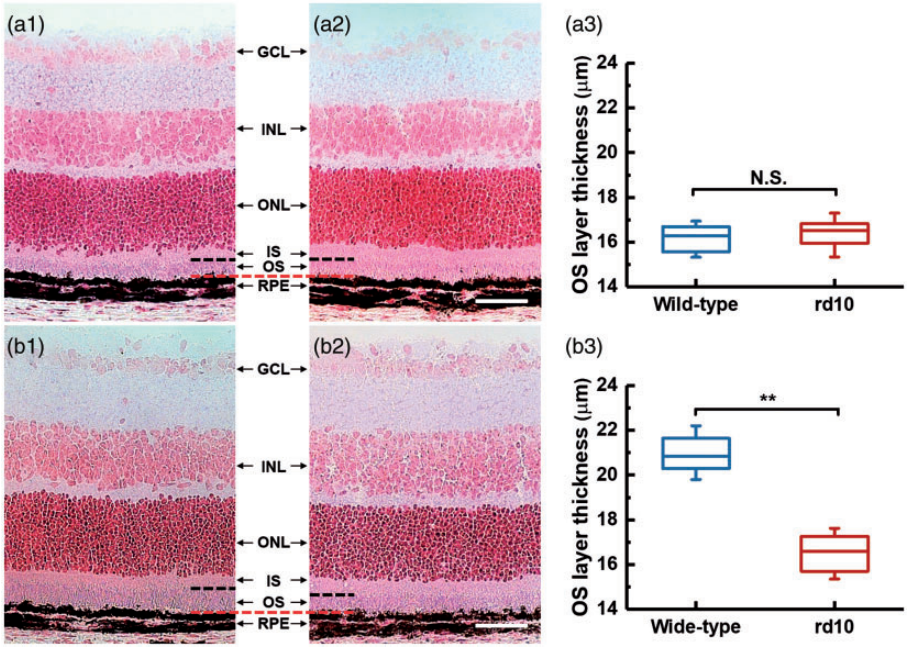

Figure 6. Histological images of eyecups from mice at P14 (a) and P16 (b). (a1) and (b1) are representative images from WT mice. (a2) and (b2) are representative images from rd10 mice. GCL: ganglion cell layer; INL: inner nuclear layer; ONL: outer nuclear layer; IS: inner segment; OS: outer segment; RPE: retinal pigment epithelium. The red- and back-dashed line represent the general positions of OS tips and IS/OS junctions, respectively. The scale bars represent 50 μm. Statistics of outer segment layer thickness in wild-type and rd10 mice at P14 (a3) and P16 (b3). Significance was determined by a two-sample *t*-test with equal variance assumed (**$P < 0.05$; NS, not significant; $n = 6$). The normality of data was determined using the Kolmogorov–Smirnov test. (A color version of this figure is available in the online journal.)

deviations about the mean in the WT group were generally similar with that in the rd10 group. Further statistical analysis about two descriptive parameters of the curves, peak amplitude and time-to-peak, confirmed that the photoreceptor-IOS responses in WT and rd10 group were similar in terms of photoreceptor-IOS magnitude and time course. The spatial spread of the photoreceptor-IOS patterns, reflected by the averaged intensity profiles (Figure 5(c1)), shows that the photoreceptor-IOS responses had a similar spatial distribution in WT and rd10 group. In comparison, previous studies demonstrated that ERG a-wave, which is tightly correlated with the activity of PDE, exhibited lower peak amplitude in rd10 mice compared with that in WT at P14.[20] Therefore, the similarities in the temporal dynamics and the spatial distribution of the photoreceptor-IOS responses between WT and rd10 groups indicate that the PDE deficiency in rd10 rods did not affect the formation of photoreceptor-IOS responses.

Previous *in vivo* IOS imaging with a high-speed OCT (1250 frames/s) has demonstrated that the photoreceptor-IOS had an onset time of ~1.1 ms, suggesting a signal origin in the early, disc-based phototransduction steps which includes the activation of rhodopsin, transducin, and PDE.[13] As the relative concentration of rhodopsin:transducin:PDE is ~100:10:1, PDE is the rate limiting factor for the disc-based phototransduction cascade.[19,27] The stimulus employed in this study has an intensity ($\sim 3.6 \times 10^9$ photon/μm^2/s) that was sufficient to activate most of the PDEs at millisecond level in both WT and rd10 rods at P14.[19,28] Our studies further demonstrated that the OS length of WT rods is similar with that of rd10 rods at P14. Previous studies also revealed that the trend of photoreceptor loss in rd10 mice was in well accordance with that in WT mice before P15, suggesting the photoreceptor densities are also similar in WT and rd10 mice at P14.[21] These results suggest that the possibility of involving OS structure-correlated variations can be minimum in our photoreceptor-IOS comparison between WT and rd10 mice at P14. If the photoreceptor-IOS responses are directly originated from or tightly correlated with the activity of PDE, we expect that a higher level of activated PDE in WT rods would contribute to a faster formation of photoreceptor-IOS responses, reflected by a steeper rising phase and a shorter time-to-peak value of the photoreceptor-IOS time courses, compared to that in the rd10 rods. However, our data show that there was no significant difference between the time-to-peak values of the photoreceptor-IOS in WT and rd10 mice (Figure 4 (b1)). Based on these results, we speculate that the photoreceptor-IOS responses have a disc-based physiological origin that is upstream from the activation of PDE in the phototransduction cascade, including the activation of rhodopsin and transducin.

In a previous OCT study, the thickness of the total retina and the photoreceptor layer (from Bruch's membrane to the inner nuclear layer/outer plexiform layer interface) showed observable difference between WT and rd10 retinas at P16.[25] Histological examination (Figure 6(b)) shows the OS lengths were reduced in rd10 group compared to that in WT group at P16. Correspondingly, the photoreceptor-IOS responses in WT and rd10 mice presented significant difference at P16 in this study. It demonstrates that the photoreceptor-IOS responses are tightly correlated with the integrity of photoreceptor and can be sensitive to the

early degeneration process due to the PDE-associated retinal degeneration.

In conclusion, our experimental study and theoretical analysis indicate that early, disc-based stages of the phototransduction cascade, which are upstream from the activation of PDE, can primarily contribute to the formation of the photoreceptor-IOS responses. The photoreceptor-IOS promises a sensitive biomarker for objective assessment of the functional integrity of retinal photoreceptors. Functional photoreceptor-IOS imaging may advance the diagnosis and treatment management of eye diseases, such as AMD and RP, which are known to damage retinal photoreceptors.

Authors' contributions: YL conducted the experiments and contributed to data analysis and manuscript preparation; TK contributed to experiments and data analysis; XY conceived the project, supervised the study, contributed to data analysis and manuscript preparation.

ACKNOWLEDGMENTS

The authors thank Mr. Xiang Shen at Lions of Illinois Eye Research Institute for the instruction of cryo-sectioning and staining.

DECLARATION OF CONFLICTING INTERESTS

The author(s) declared no potential conflicts of interest with respect to the research, authorship, and/or publication of this article.

FUNDING

This research was supported in part by NIH grants R01 EY030101, R01 EY023522, P30 EY001792; by unrestricted grant from Research to Prevent Blindness; by Richard and Loan Hill endowment.

ORCID iDs

Yiming Lu https://orcid.org/0000-0002-4895-1484
Tae-Hoon Kim https://orcid.org/0000-0002-4391-4860

REFERENCES

1. Curcio CA, Medeiros NE, Millican CL. Photoreceptor loss in age-related macular degeneration. *Invest Ophthalmol Visual Sci* 1996;**37**:1236–49
2. Nagy D, SchöNfisch B, Zrenner E, Jägle H, Long-term follow-up of retinitis pigmentosa patients with multifocal electroretinography. *Invest Ophthalmol Vis Sci* 2008;**49**:4664–71
3. Qin Y, Xu G, Wang W. Dendritic abnormalities in retinal ganglion cells of three-month diabetic rats. *Curr Eye Res* 2006;**31**:967–74
4. Scholl HP, Zrenner E. Electrophysiology in the investigation of acquired retinal disorders. *Surv Ophthalmol* 2000;**45**:29–47
5. Yao X, Wang B. Intrinsic optical signal imaging of retinal physiology: a review. *J Biomed Opt* 2015;**20**:090901
6. Hillmann D, Spahr H, Pfäffle C, Sudkamp H, Franke G, Hüttmann G. In vivo optical imaging of physiological responses to photostimulation in human photoreceptors. *Proc Natl Acad Sci U S A* 2016;**113**:13138–43
7. Yao X, Son T, Kim T-H, Lu Y. Functional optical coherence tomography of retinal photoreceptors. *Exp Biol Med* 2018;**243**:1256–64
8. Zhang F, Kurokawa K, Lassoued A, Crowell JA, Miller DT. Cone photoreceptor classification in the living human eye from photostimulation-induced phase dynamics. *Proc Natl Acad Sci U S A* 2019;**116**:7951–6
9. Bizheva K, Pflug R, Hermann B, Považay B, Sattmann H, Qiu P, Anger E, Reitsamer H, Popov S, Taylor J. Optophysiology: depth-resolved probing of retinal physiology with functional ultrahigh-resolution optical coherence tomography. *Proc Natl Acad Sci U S A* 2006;**103**:5066–71
10. Srinivasan V, Wojtkowski M, Fujimoto J, Duker J. In vivo measurement of retinal physiology with high-speed ultrahigh-resolution optical coherence tomography. *Opt Lett* 2006;**31**:2308–10
11. Schallek J, Li H, Kardon R, Kwon Y, Abramoff M, Soliz P, Ts'o D. Stimulus-evoked intrinsic optical signals in the retina: spatial and temporal characteristics. *Invest Ophthalmol Vis Sci* 2009;**50**:4865–72
12. Cooper RF, Tuten WS, Dubra A, Brainard DH, Morgan JI. Non-invasive assessment of human cone photoreceptor function. *Biomed Opt Exp* 2017;**8**:5098–112
13. Wang B, Lu Y, Yao X. In vivo optical coherence tomography of stimulus-evoked intrinsic optical signals in mouse retinas. *J Biomed Opt* 2016;**21**:09601010
14. Zhang Q, Lu R, Wang B, Messinger JD, Curcio CA, Yao X. Functional optical coherence tomography enables in vivo physiological assessment of retinal rod and cone photoreceptors. *Sci Rep* 2015;**5**:9595
15. Lu R, Levy AM, Zhang Q, Pittler SJ, Yao X. Dynamic near-infrared imaging reveals transient phototropic change in retinal rod photoreceptors. *J Biomed Opt* 2013;**18**:106013
16. Lu Y, Wang B, Pepperberg DR, Yao X. Stimulus-evoked outer segment changes occur before the hyperpolarization of retinal photoreceptors. *Biomed Opt Exp* 2017;**8**:38–47
17. Arshavsky VY, Lamb TD, Pugh EN Jr. G proteins and phototransduction. *Annu Rev Physiol* 2002;**64**:153–87
18. Lamb TD, Pugh EN Jr. Phototransduction, dark adaptation, and rhodopsin regeneration the proctor lecture. *Invest Ophthalmol Vis Sci* 2006;**47**:5137–52
19. Fu Y, Yau K-W. Phototransduction in mouse rods and cones. *Pugers Arch* 2007;**454**:805–19
20. Chang B, Hawes N, Pardue M, German A, Hurd R, Davisson M, Nusinowitz S, Rengarajan K, Boyd A, Sidney S. Two mouse retinal degenerations caused by missense mutations in the β-subunit of rod cGMP phosphodiesterase gene. *Vision Res* 2007;**47**:624–33
21. Samardzija M, Wariwoda H, Imsand C, Huber P, Heynen SR, Gubler A, Grimm C. Activation of survival pathways in the degenerating retina of rd10 mice. *Exp Eye Res* 2012;**99**:17–26
22. Barhoum R, Martinez-Navarrete G, Corrochano S, Germain F, Fernandez-Sanchez L, De la Rosa EJ, de La Villa P, Cuenca N. Functional and structural modifications during retinal degeneration in the rd10 mouse. *Neuroscience* 2008;**155**:698–713
23. Kim TH, Son T, Lu Y, Alam M, Yao X. Comparative optical coherence tomography angiography of Wild-Type and rd10 mouse retinas. *Transl Vis Sci Technol* 2018;**7**:42
24. Gargini C, Terzibasi E, Mazzoni F, Strettoi E. Retinal organization in the retinal degeneration 10 (rd10) mutant mouse: a morphological and ERG study. *J Comp Neurol* 2007;**500**:222–38
25. Pennesi ME, Michaels KV, Magee SS, Maricle A, Davin SP, Garg AK, Gale MJ, Tu DC, Wen Y, Erker LR. Long-term characterization of retinal degeneration in rd1 and rd10 mice using spectral domain optical coherence tomography. *Invest Ophthalmol Vis Sci* 2012;**53**:4644–56
26. Zhang Q-X, Zhang Y, Lu R-W, Li Y-C, Pittler SJ, Kraft TW, Yao X-C. Comparative intrinsic optical signal imaging of wild-type and mutant mouse retinas. *Opt Exp* 2012;**20**:7646–54
27. Pugh EN Jr, Lamb TD. Phototransduction in vertebrate rods and cones: molecular mechanisms of amplification, recovery and light adaptation. *Handbook Biol Phys* 2000;**3**:183–255
28. Fulton AB, Hansen RM, Findl O. The development of the rod photoresponse from dark-adapted rats. *Invest Ophthalmol Vis Sci* 1995;**36**:1038–45

(Received September 16, 2019, Accepted December 2, 2019)